Reduction of periodic motion artifacts in photoplethysmography

DOI:
10.1109/TBME.2016.2553060

Document status and date:
Published: 01/01/2017

Document Version:
Accepted manuscript including changes made at the peer-review stage

Reduction of periodic motion artifacts in photoplethysmography

Ralph W.C.G.R. Wijshoff, Massimo Mischi, *Senior Member, IEEE*, and Ronald M. Aarts, *Fellow, IEEE*

***Abstract*—Periodic motion artifacts affect photoplethysmography (PPG) signals in activities of daily living (ADL), cardiopulmonary exercise testing (CPX), and cardiopulmonary resuscitation (CPR). This hampers measurement of inter-beat-intervals (IBIs) and oxygen saturation (SpO_2). Our objective was to develop a generic algorithm to remove periodic motion artifacts, recovering artifact-reduced PPG signals for beat-to-beat analysis. Methods: The algorithm was retrospectively evaluated on forehead PPG signals measured while walking on a treadmill. The step rate was tracked in a motion reference signal via a second-order generalized-integrator with a frequency-locked loop. Two reference signals were compared: sensor motion relative to the skin ($\Delta x[n]$) measured via self-mixing interferometry, and head motion ($a_v[n]$) measured via accelerometry. The step rate was used in a quadrature harmonic model to estimate the artifacts. Quadrature components need only two coefficients per frequency leading to a short filter, and prevent undesired frequency-shifted components in the artifact estimate. Subtracting the estimate from the measured signal reduced the artifacts. Results: Compared to $\Delta x[n]$, $a_v[n]$ had a better signal-to-noise ratio and more consistently contained a component at the step rate. Artifact reduction was effective for distinct step rate and pulse rate, since the artifact-reduced signals provided more stable IBI and SpO_2 measurements. Conclusion: Accelerometry provided a more reliable motion reference signal. The proposed algorithm can be of significance for monitoring in ADL, CPX or CPR, by providing artifact-reduced PPG signals for improved IBI and SpO_2 measurements during periodic motion.**

***Index Terms*—Accelerometry, correlation cancellation, frequency-locked loop, harmonic model, inter-beat interval, least mean-squares, motion artifact reduction, oxygen saturation, photoplethysmography, pulse rate, quadrature components, second-order generalized integrator, self-mixing interferometry.**

I. INTRODUCTION

PHOTOPLETHYSMOGRAPHY (PPG) is a non-invasive easy-to-use optical technology, widely applied to monitor the cardiovascular and respiratory systems [1]–[5]. PPG measures local changes in microvascular blood volume by emitting light through tissue [6]. PPG can be used to measure cardiac pulse rate (PR) and peripheral arterial functional-hemoglobin oxygen-saturation (SpO_2) [1], [3], [5], [7]. PR can be derived from the cardiac-induced variations in a PPG signal, either in the time [8] or frequency domain [9]. An empirical calibration relates SpO_2 to the ratio of the baseline-normalized cardiac-induced variations in two PPG signals obtained at different wavelengths, typically red and near-infrared [7], [10]–[14].

PPG signals are highly susceptible to motion which hampers their use in, e.g., activities of daily living (ADL) [1], [5], [15], cardiopulmonary exercise testing (CPX) [16], [17], or cardiopulmonary resuscitation (CPR) [18], [19]. In ADL, the use of PPG is for instance researched to detect PR changes in patients with epilepsy [20], as this can indicate seizures [21]. Susceptibility to motion hampers beat-to-beat analysis, e.g., to obtain pulse rate variability (PRV) [22], or to detect atrial fibrillation [23]. Motion can also affect SpO_2 measurements, e.g., causing false positive desaturations during CPX [16], [17]. During CPR, motion artifacts due to chest compressions complicate detection of a cardiac pulse in the signal [18], [19]. In this paper, we will focus on quasi-periodic motion artifacts, which is one type of motion artifact that can occur in ADL, CPX and CPR. Quasi-periodic artifacts are furthermore relevant because algorithms may confuse them with a PR component [24].

Removal of motion artifacts to recover artifact-reduced PPG signals has been researched extensively. Various generic approaches exist for removal of additive periodic motion artifacts using correlation cancelation with an accelerometer as a motion reference [24]–[29]. In these approaches the artifact is estimated by applying a finite impulse response (FIR) filter to a single reference signal and updating all FIR-coefficients over time. However, quadrature reference signals would be preferred here, because then only two coefficients are needed per frequency and undesired frequency-shifted components cancel in the estimate [30], [31]. Wavelength-independent multiplicative optical-coupling artifacts can be removed from a PPG signal by normalization by a second PPG signal obtained at a different wavelength [32]–[34]. However, this requires a revised calibration for SpO_2. Artifact-reduced PPG signals can also be recovered using a synthetic reference for the cardiac pulse waveform [35], deriving artifact references from the measured PPG signals [36], [37], applying a signal decomposition method [38], [39], or averaging several consecutive pulses [40]. However, the approaches without an additional motion measurement provide a segmented recovery of the artifact-reduced PPG signal, require a reliable PR measurement prior to artifact removal, or need to detect the individual cardiac pulses in the corrupted PPG signal.

Methods have also been developed focussing on the extraction of averaged physiological parameters from motion-corrupted PPG signals. PR has been determined from the PPG signal frequency spectrum using an accelerometer to identify

R. Wijshoff and R. Aarts are with the Electrical Engineering Department, Eindhoven University of Technology, and with Philips Research, Eindhoven, the Netherlands (e-mail: {r.w.c.g.r.wijshoff, r.m.aarts}@tue.nl, {ralph.wijshoff, ronald.m.aarts}@philips.com).

M. Mischi is with the Electrical Engineering Department, Eindhoven University of Technology, Eindhoven, the Netherlands (e-mail: m.mischi@tue.nl).

the motion frequencies [41]–[44]. In [44], an artifact-reduced PPG time-trace is also reconstructed, but the reconstruction is window-based, and uses per window a single PR selected from the PPG frequency spectrum. PR has also been determined from the PPG signal frequency spectrum after artifact removal with a notch filter at the motion frequency as measured via the photodiode with the LEDs switched off [45]. Motion-robust SpO_2 measurements have been obtained by discriminating cardiac-induced arterial and motion-induced venous components based on their different amplitude ratios in the red and near-infrared PPG signals [46], [47]. PR and SpO_2 can also be measured more reliably by using the smoothed pseudo Wigner-Ville distribution [48].

In this paper, we focus on a generic approach to remove periodic motion artifacts to recover artifact-reduced PPG signals for beat-to-beat analysis. We determined the fundamental motion frequency from a motion reference signal via a second-order generalized integrator (SOGI) with a frequency-locked loop (FLL) [49]. We described the motion artifact by a harmonic model of quadrature components with frequencies related to the fundamental motion frequency. With quadrature components only two coefficients need to be estimated per frequency component, leading to a short filter. We estimated the coefficients via a least mean-squares (LMS) algorithm. Quadrature components also prevent undesired frequency-shifted components in the artifact estimate. The motion artifact was removed by subtracting the harmonic model from the measured PPG signal. Furthermore, we compare two motion reference signals: sensor motion relative to the skin and body motion. Motion relative to the skin is an origin of artifacts in PPG [1], [7], [26], [32], [33], [35]. We measured relative sensor motion with a laser diode attached to the PPG sensor using self-mixing interferometry (SMI) [50]–[52]. The objective was to gain insight in the amount of relative sensor motion. We measured body motion with an accelerometer. Red and infrared (IR) PPG signals were measured on the forehead while walking on a treadmill to generate periodic motion artifacts. We used a reflective PPG sensor, because measurement of relative motion is more convenient compared to a transmissive sensor. Furthermore, a reflective sensor is more widely applicable than a transmissive sensor [5], [11], [53], [54]. We performed a preliminary validation of the algorithm only, using a limited data set of thirty measurements obtained from six healthy volunteers.

II. Methods A: Experiment and measurements

Thirty measurements were performed on six healthy male volunteers, following the protocol in Fig. 1a. Each subject walked on a treadmill at speeds of 4, 5, 6, 7 and 8 km/h to generate periodic motion artifacts. Each speed was maintained for 2 min, and was preceded and followed by 1-min of rest with the subject standing still. The institutional review board approved the study. All subjects signed informed consent.

Fig. 1b shows the customized forehead sensor. Raw red (660 nm) and near-infrared (900 nm) PPG signals were obtained with a forehead reflectance pulse oximetry sensor (Nellcor™ Oxisensor II RS-10, Covidien-Nellcor™, Dublin,

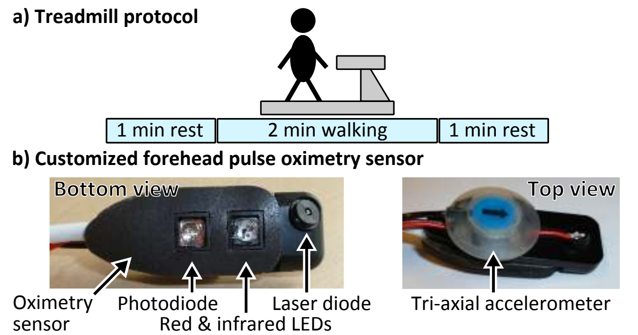

Fig. 1. (a) Treadmill protocol to generate periodic motion artifacts. (b) Forehead pulse oximetry sensor with laser diode and tri-axial accelerometer as motion references. LED: light emitting diode.

Ireland), controlled by a custom-built photoplethysmograph. The headband delivered with the oximetry sensor was used to exert pressure on the sensor. An 850-nm vertical-cavity surface-emitting laser diode (LD) with an internal monitor diode (ULM-Photonics GmbH, Philips, Ulm, Germany) was positioned next to the oximetry sensor to measure sensor motion relative to the skin. As Fig. 1b shows, the LD was positioned at an angle of 45° in the plane of the oximetry sensor and at an angle of 30° with respect to the surface normal, to allow measuring vertical and horizontal relative sensor motion. The laser light was focussed onto the skin via a ball lens integrated into the LD package. A tri-axial accelerometer (LIS344ALH, STMicroelectronics, Geneva, Switzerland) was placed on top of the oximetry sensor to measure head motion. A lead I electrocardiography (ECG) signal was recorded as a reference, using a custom-built ECG module. The PPG, accelerometry, monitor diode and ECG signals were simultaneously recorded using a 16 bit digital data acquisition card (DAQ) (NI USB-6259, National Instruments, Austin, TX, USA). A LabVIEW (National Instruments, Austin, TX, USA) program controlled the DAQ. A finger clip pulse oximetry sensor (M1191B, Philips Medizin Systeme Boeblingen GmbH, Boeblingen, Germany) was used with a commercial pulse oximetry OEM board to obtain SpO_2 measurements for comparison.

III. Methods B: Artifact reduction algorithm

Fig. 2 shows the generic motion artifact reduction algorithm which ran at a sampling rate of $f_s = 250$ Hz. The primary input was the measured red or IR PPG signal, $ppg[n]$ [V], with sample index n. The algorithm was run once for the red PPG signal, and once for the IR PPG signal. The secondary input was the motion reference signal, $m_{\mathrm{ref}}[n]$, used to track the fundamental motion frequency, which was the step rate. We compared two motion reference signals: sensor motion relative to the skin measured via SMI (Sec. III-A), and head motion derived from the accelerometer (Sec. III-B). The primary and secondary input signals were preprocessed by a band-pass filter (BPF) (Sec. III-C). The fundamental motion frequency, $\omega_{\mathrm{FLL}}[n]$ [rad/s], was estimated from $m_{\mathrm{ref}}[n]$ using a SOGI-based structure with an FLL (Sec. III-D). The motion artifact was subsequently estimated and removed by constructing

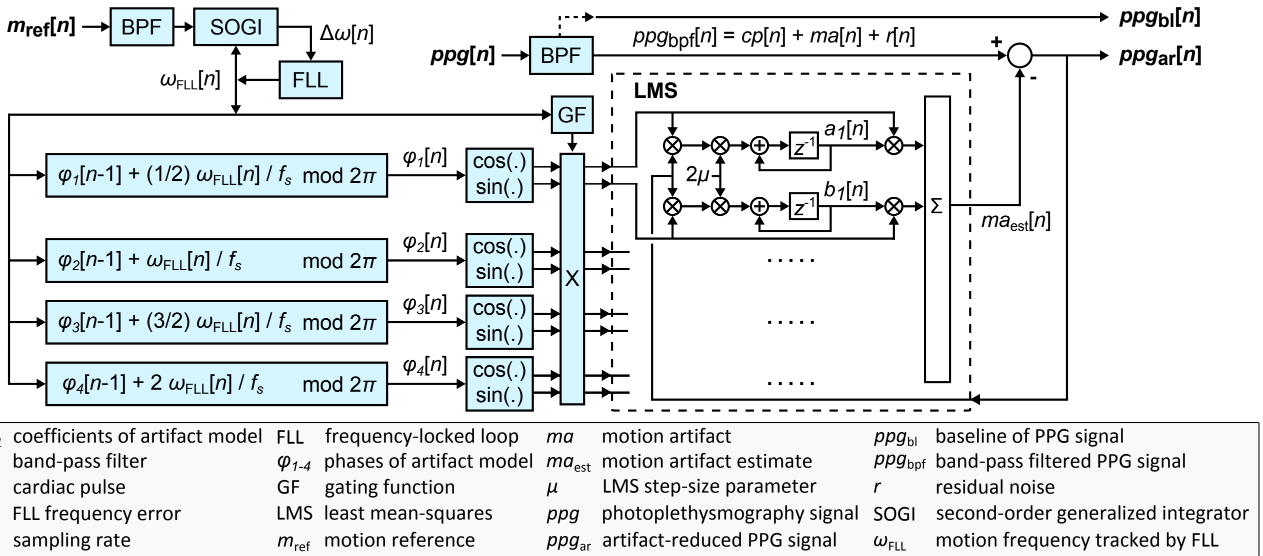

Fig. 2. Overview of the motion artifact reduction algorithm. The primary input is the red or infrared PPG signal, $ppg[n]$. The algorithm runs once for each of the PPG signals. The secondary input is the motion reference signal, $m_{\mathrm{ref}}[n]$. The primary and secondary inputs are preprocessed with a BPF. After the BPF, the PPG signal $ppg_{\mathrm{bpf}}[n]$ is assumed a sum of a cardiac pulse component, $cp[n]$, a motion artifact, $ma[n]$, and residual noise, $r[n]$. The BPF also extracts the baseline of the PPG signal, $ppg_{\mathrm{bl}}[n]$. A SOGI-based structure with an FLL tracks the fundamental frequency of motion, $\omega_{\mathrm{FLL}}[n]$, in $m_{\mathrm{ref}}[n]$. This frequency is used to construct the phases $\phi_{1-4}[n]$ of four cosine and sine quadrature components, which are the basis of the artifact model. An LMS algorithm with step-size parameter μ determines the amplitudes $a_{1-4}[n]$ and $b_{1-4}[n]$ of the cosine and sine quadrature components, respectively, and sums these components to construct the motion artifact estimate, $ma_{\mathrm{est}}[n]$. Subtracting $ma_{\mathrm{est}}[n]$ from $ppg_{\mathrm{bpf}}[n]$ yields the artifact-reduced output signal, $ppg_{\mathrm{ar}}[n]$. The artifact removal stage is switched on by the GF only if the tracked motion frequency $\omega_{\mathrm{FLL}}[n]$ is considered stable. BPF: band-pass filter; FLL: frequency-locked loop; GF: gating function; LMS: least mean-squares; PPG: photoplethysmography; SOGI: second-order generalized integrator.

quadrature reference signals and applying an LMS algorithm (Sec. III-E). The algorithm output was the artifact-reduced PPG signal, $ppg_{\mathrm{ar}}[n]$.

A. Relative sensor motion

We measured motion of the oximetry sensor relative to the skin, because we expected that relative sensor motion would change the tissue volume which is illuminated by the LEDs, resulting in a motion artifact. Therefore, we expected a good correlation between relative sensor motion and motion artifacts in the PPG signals.

Relative sensor motion was measured with the LD using SMI. Relative sensor motion caused a Doppler shift in the emitted laser light. The monitor diode of the LD measured a signal at the Doppler frequency when back-scattered laser light entered the laser cavity and interfered with the standing wave. We determined a measure of sensor motion relative to the skin from the monitor diode signal.

A DC laser current of about 1.63 mA generated about 0.5 mW of optical output power. The laser current was sinusoidally modulated at a frequency of 40 kHz with an amplitude of 158 μA. The modulation resulted in quadrature Doppler frequency components around the modulation frequency and its first harmonic, respectively, as was measured by the monitor diode. The DAQ sampled the 100 kHz band-limited monitor diode signal at a sampling rate of 200 kHz.

The remainder of this section summarizes the determination of relative sensor motion. More details can be found in [51].

Baseband quadrature Doppler signals were obtained by translating the Doppler signals around the modulation frequency and its harmonic to baseband and applying a 15-kHz low-pass filter (LPF) and a 10-Hz high-pass filter (HPF). The baseband Doppler signals were normalized via the Hilbert transform, by using the Doppler phase of the resulting analytical signals, $\phi_d[n]$ [rad], in a sine and a cosine. This resulted in the normalized Doppler signals $y[n]$ and $x[n]$:

$$y[n] = \sin\left(\phi_d[n]\right), \tag{1}$$

$$x[n] = \cos\left(\phi_d[n]\right). \tag{2}$$

Relative sensor motion, $\Delta x[n]$, was then obtained via

$$\Delta x[n] = \frac{1}{2\pi}\mathrm{unwrap}\left[\mathrm{atan2}\left(\frac{y[n]}{x[n]}\right)\right], \tag{3}$$

where unwrap removes the discontinuities in the radian phase by adding multiples of $\pm 2\pi$, and atan2 is a four-quadrant arctangent implementation. After the LPF of the preprocessing stage (Sec. III-C), $\Delta x[n]$ was down-sampled to $f_s = 250$ Hz.

The unit of $\Delta x[n]$ (3) was the number of Doppler cycles. The absolute unit could not be determined because the angle between the laser beam and the skin was unknown and because a three-dimensional motion was mapped onto a single axis.

B. Accelerometry

The tri-axial accelerometer measured head motion. From the three axes, the head-vertical axis $a_v[n]$ contained the strongest fundamental motion-frequency component, and was therefore used as motion reference $m_{\mathrm{ref}}[n]$.

C. Preprocessing

As preprocessing, the same BPF was applied to $ppg[n]$ and $m_{\mathrm{ref}}[n]$. The BPF was an LPF followed by a linear-phase HPF.

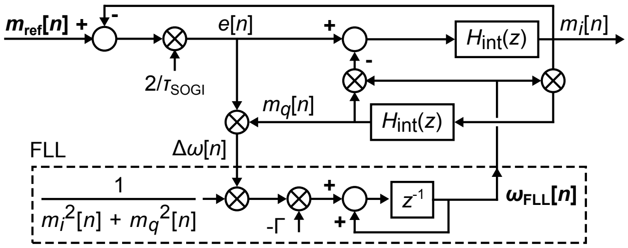

Fig. 3. The motion frequency, $\omega_{\mathrm{FLL}}[n]$, is tracked in the motion reference signal, $m_{\mathrm{ref}}[n]$, via a SOGI-based structure with an FLL. The integrators $H_{\mathrm{int}}(z)$ of the SOGI filter from the input $m_{\mathrm{ref}}[n]$ the outputs $m_i[n]$ and $m_q[n]$, the in-phase and quadrature signals at $\omega_{\mathrm{FLL}}[n]$, respectively. The time-constant τ_{SOGI} [s] sets the filter bandwidth. The FLL input, $\Delta\omega[n] = e[n] \cdot m_q[n]$ with $e[n] = 2(m_{\mathrm{ref}}[n] - m_i[n])/\tau_{\mathrm{SOGI}}$, is a measure of the FLL frequency error and is used to adjust the FLL output $\omega_{\mathrm{FLL}}[n]$. The FLL gain Γ [-] sets the FLL bandwidth. FLL: frequency-locked loop; SOGI: second-order generalized integrator.

A sixth-order Butterworth 4-Hz LPF removed high-frequency noise. To construct the HPF, the low-frequency baseline was first extracted via a filter with impulse response

$$h_{\mathrm{bl}}[n] = \frac{\sin\left(2\pi f_c \left(n - N_{\mathrm{bl}}\right)/f_s\right)}{2\pi f_c \left(n - N_{\mathrm{bl}}\right)/f_s} \frac{w_H[n]}{S_{\mathrm{hbl}}},\ n = 0, ..., 2N_{\mathrm{bl}}, \tag{4}$$

with cut-off frequency $f_c = 0.5$ Hz, Hamming window $w_H[n]$ centered at $n = N_{\mathrm{bl}}$, normalization factor S_{hbl} to have $h_{\mathrm{bl}}[n]$ sum to 1, and $N_{\mathrm{bl}} = f_s/f_c = 500$ samples. The HPF was obtained by subtracting the baseline from the original signal delayed by N_{bl} samples. The sinc-function in (4) assured a linear phase-response. The Hamming window reduced overshoot and ringing in the magnitude frequency-response. The extracted PPG signal baselines, $ppg_{\mathrm{bl}}[n]$, were used to determine pulsatility (Sec. IV-C) and SpO_2 (Sec. IV-E).

D. Measurement of the step rate

Fig. 3 shows the SOGI-based structure with the FLL [49], [55], [56] used to track the step rate in $m_{\mathrm{ref}}[n]$ on a sample-to-sample basis. The SOGI has two integrators, $H_{\mathrm{int}}(z)$, which filtered from the input $m_{\mathrm{ref}}[n]$ the outputs $m_i[n]$ and $m_q[n]$, the in-phase and quadrature signals at FLL frequency $\omega_{\mathrm{FLL}}[n]$ [rad/s], respectively. The FLL used $m_i[n]$ and $m_q[n]$ to estimate the frequency error between $\omega_{\mathrm{FLL}}[n]$ and the step rate, $\Delta\omega[n]$, and to make the FLL adaptation speed independent of the magnitude of the tracked frequency component. We assumed step rates between 1 and 3 Hz.

The transfer functions from $m_{\mathrm{ref}}[n]$ to $m_i[n]$ and $m_q[n]$ are, respectively, using continuous-time for simplicity,

$$H_i(s) = \frac{(2/\tau_{\mathrm{SOGI}})s}{s^2 + (2/\tau_{\mathrm{SOGI}})s + \omega_{\mathrm{FLL}}^2}, \tag{5}$$

$$H_q(s) = \frac{(2/\tau_{\mathrm{SOGI}})\omega_{\mathrm{FLL}}}{s^2 + (2/\tau_{\mathrm{SOGI}})s + \omega_{\mathrm{FLL}}^2}, \tag{6}$$

with $s = j\omega$, time-constant τ_{SOGI} [s], and FLL frequency ω_{FLL} [rad/s] which has been assumed constant here. Frequency ω_{FLL} is the resonance of (5) and (6), where the input appears unchanged at $m_i[n]$ and with a 90° lag at $m_q[n]$. The zero of the transfer function from $m_{\mathrm{ref}}[n]$ to $e[n]$ shows that loop input $e[n]$ contains no component at ω_{FLL}:

$$H_e(s) = \frac{H_q(s)}{\omega_{\mathrm{FLL}}}\left(s^2 + \omega_{\mathrm{FLL}}^2\right). \tag{7}$$

The 3-dB frequencies f_{cSOGI} [Hz] around the resonances of (5) and (6) describe the bandwidth of the filter:

$$f_{\mathrm{cSOGI}} = \frac{1}{2\pi}\sqrt{\omega_{\mathrm{FLL}}^2 + \frac{2}{\tau_{\mathrm{SOGI}}^2} \pm \frac{2}{\tau_{\mathrm{SOGI}}}\sqrt{\omega_{\mathrm{FLL}}^2 + \frac{1}{\tau_{\mathrm{SOGI}}^2}}}. \tag{8}$$

We used $\tau_{\mathrm{SOGI}} = 0.7$ s, giving a 3-dB width of about 0.5 Hz.

We implemented $H_{\mathrm{int}}(z)$ as a second-order integrator [55] to accurately approximate an ideal integrator $1/(j\omega)$ for the assumed motion frequencies up to 3 Hz:

$$H_{\mathrm{int}}(z) = \frac{T_s}{2}\frac{3z^{-1} - z^{-2}}{1 - z^{-1}}. \tag{9}$$

Compared to an ideal integrator for frequencies up to 3 Hz, the deviation in magnitude and phase frequency response of (9) was at most 0.24% and $-0.006°$, respectively. The delays in the numerator of (9) prevented an algebraic loop.

The FLL adjusted $\omega_{\mathrm{FLL}}[n]$ to track the frequency $\omega_{\mathrm{ref}}[n]$ in $m_{\mathrm{ref}}[n]$. The FLL input, $\Delta\omega[n] = e[n] \cdot m_q[n]$, is an instantaneous measure of the frequency error $\omega_{\mathrm{FLL}}[n] - \omega_{\mathrm{ref}}[n]$. As (7) shows, $e[n]$ and $m_q[n]$ have the same phase when $\omega_{\mathrm{FLL}}[n] > \omega_{\mathrm{ref}}[n]$ and opposite phase when $\omega_{\mathrm{FLL}}[n] < \omega_{\mathrm{ref}}[n]$. Therefore, $\Delta\omega[n]$ is on average positive when $\omega_{\mathrm{FLL}}[n]$ should decrease, and on average negative when $\omega_{\mathrm{FLL}}[n]$ should increase. Multiplying $\Delta\omega[n]$ by the negative FLL gain $-\Gamma$ [-] resulted in a frequency correction which steered $\omega_{\mathrm{FLL}}[n]$ towards $\omega_{\mathrm{ref}}[n]$. The input $\Delta\omega[n]$ was normalized by $m_i^2[n] + m_q^2[n]$ to make the adaptation speed independent of the magnitude of the tracked frequency component. When $m_i^2[n] + m_q^2[n] = 0$, normalization was not performed and $\omega_{\mathrm{FLL}}[n]$ was not updated. When $m_i^2[n] + m_q^2[n] > 0$, $\omega_{\mathrm{FLL}}[n]$ was adjusted according to the following approximation for $\omega_{\mathrm{FLL}}[n] \approx \omega_{\mathrm{ref}}[n]$, by using $\omega_{\mathrm{FLL}}^2[n] - \omega_{\mathrm{ref}}^2[n] \approx 2\omega_{\mathrm{FLL}}[n](\omega_{\mathrm{FLL}}[n] - \omega_{\mathrm{ref}}[n])$ in (7):

$$\omega_{\mathrm{FLL}}[n+1] = (1 - \Gamma)\,\omega_{\mathrm{FLL}}[n] + \Gamma\omega_{\mathrm{ref}}[n], \tag{10}$$

where we neglected the double-frequency component in $\Delta\omega[n]$. The relation between FLL gain Γ, time-constant τ_{FLL} [s], and 3-dB cut-off frequency f_{cFLL} [Hz] follows from (10):

$$\Gamma = 1 - \exp\left(\frac{-1}{\tau_{\mathrm{FLL}} f_s}\right) = 1 - \exp\left(\frac{-2\pi f_{\mathrm{cFLL}}}{f_s}\right). \tag{11}$$

We used $f_{\mathrm{cFLL}} = 0.1$ Hz ($\tau_{\mathrm{FLL}} \approx 1.6$ s) so (10) suppressed the minimum 2-Hz double-frequency component by a factor of 20. We initiated the FLL at $\omega_{\mathrm{FLL}}[0]/(2\pi) = 1.5$ Hz.

The SOGI-based structure in Fig. 3 locked to the frequency in $m_{\mathrm{ref}}[n]$ which was closest to $\omega_{\mathrm{FLL}}[n]$ at start-up or after a temporary loss of signal in $m_{\mathrm{ref}}[n]$. It could therefore lock to a (sub-)harmonic of the step rate. To ascertain locking to the step rate, $\omega_{\mathrm{FLL}}[n]$ was for each n compared to the frequency $f_{\max}$ of the largest local maximum between 1 and 3 Hz in the magnitude frequency spectrum of $m_{\mathrm{ref}}[n]$. Once per second, a coarse spectrum of $m_{\mathrm{ref}}[n]$ was determined via the Fast Fourier Transform of a 5 s window and $f_{\max}$ was updated.

If $\omega_{\mathrm{FLL}}[n]/(2\pi)$ deviated by more than 0.5 Hz from $f_{\max}$, then $\omega_{\mathrm{FLL}}[n]$ was replaced by $2\pi f_{\max}$ to lock to the step rate, otherwise $\omega_{\mathrm{FLL}}[n]$ remained unchanged. Frequency $f_{\max}$ was updated as unavailable if no local maximum was found, and then $\omega_{\mathrm{FLL}}[n]$ remained unchanged too.

E. Estimation and reduction of motion artifacts

We described the band-pass filtered signal, $ppg_{\mathrm{bpf}}[n]$, obtained by applying the BPF in Sec. III-C to the measured signal $ppg[n]$, as a sum of a cardiac pulse component, $cp[n]$, a motion artifact, $ma[n]$, and residual noise, $r[n]$:

$$ppg_{\mathrm{bpf}}[n] = cp[n] + ma[n] + r[n]. \tag{12}$$

We chose an additive model, because spectral analysis of $ppg_{\mathrm{bpf}}[n]$ showed that walking introduced components at the step rate and its (sub-)harmonics in $ppg_{\mathrm{bpf}}[n]$ in addition to components at the PR and its harmonics. Subtracting the motion artifact estimate $ma_{\mathrm{est}}[n]$ from $ppg_{\mathrm{bpf}}[n]$ gave the artifact-reduced signal $ppg_{\mathrm{ar}}[n]$:

$$ppg_{\mathrm{ar}}[n] = ppg_{\mathrm{bpf}}[n] - ma_{\mathrm{est}}[n]. \tag{13}$$

We obtained $ma_{\mathrm{est}}[n]$ via a quadrature harmonic model:

$$\mathrm{ma}_{\mathrm{est}}[n] = G[n] \sum_{k=1}^{4} \left[a_k[n] \cos\left(\phi_k[n]\right) + b_k[n] \sin\left(\phi_k[n]\right)\right], \tag{14}$$

with gating function $G[n]$ [-], amplitudes $a_k[n]$ and $b_k[n]$ [V] and motion phases $\phi_k[n]$ [rad]. Motion artifact $ma_{\mathrm{est}}[n]$ was separately estimated for the red and IR PPG signal. $G[n]$ assessed the stability of $\omega_{\mathrm{FLL}}[n]$. $G[n]$ was one when $\omega_{\mathrm{FLL}}[n]$ was considered stable, and zero otherwise. $G[n]$ forced $ma_{\mathrm{est}}[n]$ to zero when no stable motion frequency was detected. We determined $G[n]$ via hysteresis detection:

$$df_{\mathrm{FLL}}[n] = \frac{f_s}{2\pi} H_G(z) \left|\omega_{\mathrm{FLL}}[n] - \omega_{\mathrm{FLL}}[n-1]\right|, \tag{15}$$

$$G_h[n] = \begin{cases} 0 \to 1 \text{ if } df_{\mathrm{FLL}}[n] < 0.1 \text{ Hz/s} \\ 1 \to 0 \text{ if } df_{\mathrm{FLL}}[n] > 0.5 \text{ Hz/s} \end{cases}, \tag{16}$$

$$G[n] = H_G(z) G_h[n], \tag{17}$$

$$H_{G(z)} = \frac{1 - \exp(-1/(\tau_G f_s))}{z - \exp(-1/(\tau_G f_s))}, \tag{18}$$

with $\tau_G = 0.2$ s. $H_G(z)$ tracked the envelope in (15) and smoothed in (17). We initialized $G_h[n]$ at 0. The phases $\phi_k[n]$ [rad] were determined as:

$$\phi_k[n] = \phi_k[n-1] + \frac{k\omega_{\mathrm{FLL}}[n]}{2f_s} \bmod 2\pi, k = 1, 2, 3, 4, \tag{19}$$

where mod is the modulo operation. Phases were reset to $\phi_k[n] = 0$ when $G[n] < 0.005$. The amplitudes $a_k[n]$ and $b_k[n]$ were estimated via an LMS algorithm [30], [57]:

$$a_k[n+1] = a_k[n] + 2\mu G[n] ppg_{\mathrm{ar}}[n] \cos\left(\phi_k[n]\right), \tag{20}$$

$$b_k[n+1] = b_k[n] + 2\mu G[n] ppg_{\mathrm{ar}}[n] \sin\left(\phi_k[n]\right), \tag{21}$$

with step-size parameter μ. Coefficients were reset to $a_k[n] = 0$ and $b_k[n] = 0$ when $G[n] < 0.005$. The LMS-filter transfer-function between $ppg_{\mathrm{bpf}}[n]$ and $ppg_{\mathrm{ar}}[n]$ can be approximated by a cascade of notch filters at $(k/2)\omega_{\mathrm{FLL}}$ [30], [57], where each notch has a 3-dB bandwidth W [Hz] of about [30]

$$W \approx \frac{\mu f_s}{\pi}. \tag{22}$$

Furthermore, μ determined the convergence time T_{cv} [s] to a fraction $0 < v < 1$ of the targeted values for a_k and b_k via

$$T_{cv} = \frac{1}{f_s} \frac{\ln(1-v)}{\ln(1-\mu)}. \tag{23}$$

Removal of pulses with a PR close to the step rate was limited to ranges of about $(k\omega_{\mathrm{FLL}})/(4\pi) \pm 1/24$ Hz by using $\mu = 0.001$, so $W \approx 0.08$ Hz ≈ 4.8 min^{-1}, and $T_{c0.95} \approx 12$ s.

IV. Methods C: Performance evaluation

The performance of the artifact reduction was assessed for both relative sensor motion $\Delta x[n]$ and head motion $a_v[n]$. The adequacy as motion reference was assessed by the signal-to-noise ratio (SNR) and the stability of the extracted motion frequency (section IV-A). The artifact-reduced PPG signal was assessed for accuracy of the inter-beat intervals (IBIs) compared to the ECG R-peak intervals (sections IV-B, IV-C and IV-D), and for accuracy of SpO_2 (section IV-E).

A. Motion references

The SNR of the motion references was determined as the ratio of the root mean square (RMS) amplitude during walking and rest. The RMS amplitude was determined from $\Delta x_{\mathrm{bpf}}[n]$ and $a_{v\_\mathrm{bpf}}[n]$, as obtained by applying the BPF in Sec. III-C to $\Delta x[n]$ and $a_v[n]$, respectively. Episodes with outliers in $\Delta x_{\mathrm{bpf}}[n]$ and $a_{v\_\mathrm{bpf}}[n]$, caused by touching the head band, were excluded. The stability of $f_{\mathrm{FLL}} = \omega_{\mathrm{FLL}}/(2\pi)$ was assessed for $\Delta x[n]$ and $a_v[n]$ in each 2 min walking period by the standard deviation (SD) of f_{FLL} excluding the first 10 s, and the mean and SD of $df_{\mathrm{FLL}}[n]$ and $G[n]$.

B. R-peak detection

As a reference for the IBIs we used the R-peak to R-peak intervals (RRIs) in the ECG signal, which was sampled at 250 Hz and band-limited to 0.5-20 Hz. We detected the steepest ascent and descent of the QR and RS slopes, respectively, by applying positive and negative thresholds to the ECG signal time-derivative. The initial R-peak was found as the maximum in the ECG signal between the QR and RS slopes. The time instant of the i^{th} R-peak, $t_R[i]$, was found by interpolating the initial R-peak and its neighbouring samples with a second-order polynomial. All detected R-peaks were visually inspected. The RRI was determined from the interpolated time instants as $RRI[i] = t_R[i] - t_R[i-1]$.

C. Pulse detection

Pulses were detected in the red and IR band-pass filtered signal $ppg_{\mathrm{bpf}}[n]$ and artifact-reduced signal $ppg_{\mathrm{ar}}[n]$. In the following list we use $ppg_{\mathrm{bp}}[n]$ to represent one of these four signals. Pulse detection comprised of the following steps:

- The index of the systolic slope n_{sl} was found as the positive-to-negative zero-crossing in $ppg_{\mathrm{bp}}[n]$.

- The index of the diastolic level n_{dias} was found as the positive-to-negative zero-crossing in the time-derivative of $ppg_{\mathrm{bp}}[n]$ directly preceding n_{sl}.
- The index of the systolic level n_{sys} was found as the negative-to-positive zero-crossing in the time-derivative of $ppg_{\mathrm{bp}}[n]$ directly following n_{sl}.
- A set of pulse candidates was formed for all n_{sl} which had both an associated n_{dias} and n_{sys}.
- Pulse candidates with a pulsatility plt smaller than a threshold plt_{thr} were omitted. For each pulse, we defined

$$plt = 10^3 \cdot \left(\frac{ppg_{\mathrm{bp}}[n_{\mathrm{dias}}]}{ppg_{\mathrm{bl}}[n_{\mathrm{dias}}]} - \frac{ppg_{\mathrm{bp}}[n_{\mathrm{sys}}]}{ppg_{\mathrm{bl}}[n_{\mathrm{sys}}]} \right). \tag{24}$$

  The threshold plt_{thr} was empirically chosen as 70% of the average pulsatility of all pulse candidates detected in the 10 s prior to the walking period, i.e., plt_{thr} was adapted to each individual measurement.
- From the remaining pulse candidates we only kept pairs of red and IR pulses which we could associate with an R-peak. We associated a pulse pair with an R-peak at time instant $t_R[i]$, if the time instants of their diastolic levels were between $t_R[i]$ and $t_R[i+1]$. If multiple red or IR pulses occurred between $t_R[i]$ and $t_R[i+1]$, the one closest to $t_R[i]$ was selected and the others were omitted. An R-peak at $t_R[i]$ had no associated pulse pair if the red or IR pulse was missing between $t_R[i]$ and $t_R[i+1]$.
- The systolic and diastolic levels and their time instants of the pulses associated with R-peaks were finally found by interpolating the initial detections and their neighbouring samples with a second-order polynomial.

We assessed pulse detection during walking by the percentage p_A of initial pulse candidates that was associated with an R-peak. We compared p_A before and after artifact reduction.

D. Inter-beat intervals

The artifact-reduced signal $ppg_{\mathrm{ar}}[n]$ was assessed for IBI accuracy. IBIs were determined as the time difference between the interpolated systolic points of subsequent IR PPG pulses which were associated with R-peaks. For R-peaks without associated pulse pair, the involved IBIs were ignored. The IBI accuracy was determined as the difference with the associated RRI:

$$\Delta IBI[i] = IBI[i] - RRI[i], \tag{25}$$

with i referring to the i^{th} IBI. We assessed the algorithm performance by the 10^{th} to 90^{th} percentile of ΔIBI for each measurement during rest, walking, and after artifact reduction. The interpolation in the R-peak and pulse detection assured that ΔIBI was not restricted to integer multiples of 4 ms.

E. Oxygen saturation

The artifact-reduced signal $ppg_{\mathrm{ar}}[n]$ was also assessed for $\mathrm{SpO_2}$ accuracy. For pulse pairs associated with an R-peak, $\mathrm{SpO_2}$ was obtained via the calibration curve of the oximetry sensor:

$$\mathrm{SpO_2} = a\rho^2 + b\rho + c, \tag{26}$$

with calibration coefficients a [%], b [%] and c [%], and ratio-of-ratios ρ [-]. The ratio-of-ratios was determined as

$$\rho = (AC_{\mathrm{rd}}/DC_{\mathrm{rd}}) \,/\, (AC_{\mathrm{ir}}/DC_{\mathrm{ir}}), \tag{27}$$

in which pulse magnitude AC [V] was the difference between the interpolated diastolic and systolic levels, pulse mean DC [V] was the average of $ppg_{\mathrm{bl}}[n]$ between the interpolated time instants of the diastolic and systolic points, and subscripts rd and ir refer to the red and IR PPG signal, respectively. An 0.1 change in ρ corresponded to a 3-4% change in $\mathrm{SpO_2}$.

We assessed the algorithm performance by the 10^{th} to 90^{th} percentile range of $\mathrm{SpO_2}$ during rest, walking, and after artifact reduction. We compared the median $\mathrm{SpO_2}$ obtained from (26) during rest and after artifact reduction to the median $\mathrm{SpO_2}$ obtained during rest with the commercial device. No beat-to-beat comparison was made, because of differences in blood flow time from the lungs to the forehead and the finger, and because of low-pass filtering in the commercial device.

V. Results

A. Motion artifact references

The relative sensor motion $\Delta x[n]$ and the head motion $a_v[n]$ are evaluated in Fig. 4 and Table I. Fig. 4a and b show the RMS-amplitudes of $\Delta x_{\mathrm{bpf}}[n]$ and $a_{v\_\mathrm{bpf}}[n]$, respectively, for each measurement during rest (dots) and walking (circles). Across the subjects, $a_{v\_\mathrm{bpf}}[n]$ behaved more consistently than $\Delta x_{\mathrm{bpf}}[n]$, and $a_{v\_\mathrm{bpf}}[n]$ had a better SNR than $\Delta x_{\mathrm{bpf}}[n]$. Table I quantifies the SNR as the ratio of the RMS-amplitude during walking and rest. The average ratio was about 82 for $a_{v\_\mathrm{bpf}}[n]$, and about 6 for $\Delta x_{\mathrm{bpf}}[n]$.

Fig. 4c and d show the mean (open triangle / square) and SD (filled triangle / square) of $df_{\mathrm{FLL}}[n]$ (15) for $\Delta x[n]$ and $a_v[n]$, respectively. These are smaller and more consistent for $a_v[n]$. Table I shows the f_{FLL} SD. This is also smaller and more consistent for $a_v[n]$. The mean f_{FLL} SD was about 2 min^{-1} for $a_v[n]$ and about 17 min^{-1} for $\Delta x[n]$. The FLL thus tracked the step rate more steadily in $a_v[n]$ than in $\Delta x[n]$.

Fig. 4e and f show the mean (open triangle / square) and SD (filled triangle / square) of $G[n]$ for $\Delta x[n]$ and $a_v[n]$, respectively. The mean was consistently about 1 for $a_v[n]$, whereas it fluctuated for $\Delta x[n]$. For $\Delta x[n]$, a decrease in mean and an increase in SD of $G[n]$ was due to unstable tracking of the step rate, as shown by an increase in $df_{\mathrm{FLL}}[n]$. In these cases, the most prominent spectral component over time in $\Delta x[n]$ did not occur at the step rate. Instead, the most prominent spectral component varied between the step rate and its (sub)harmonic, or the spectral activity was unstructured.

Table I also shows for $a_v[n]$ that subject 3 has an approximately twofold f_{FLL} SD compared to the other subjects, indicating a larger step rate variation for subject 3.

B. Motion artifact reduction

The time traces in Fig. 5 exemplify the effect of walking and artifact reduction on the PPG signal, IBIs, and $\mathrm{SpO_2}$. Walking caused $ppg_{\mathrm{bpf}}[n]$ in Fig. 5a to vary periodically, where destructive interference by the artifact caused fading of the signal. The artifact estimate $ma_{\mathrm{est}}[n]$ in Fig. 5b was

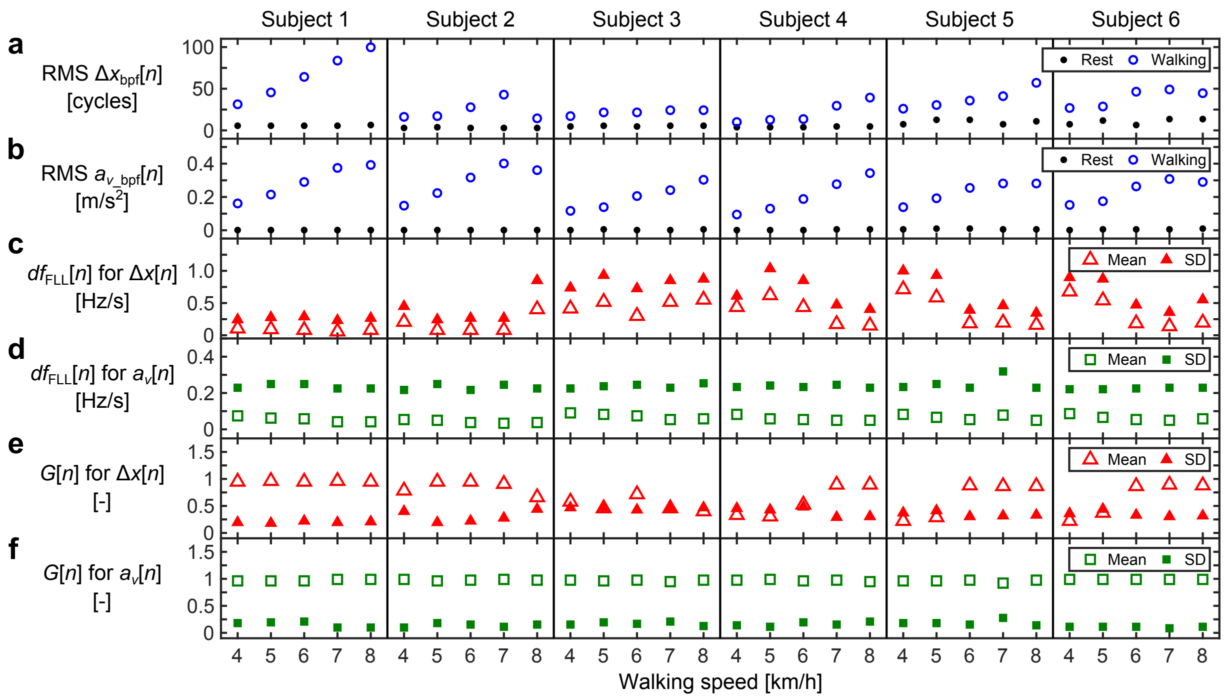

Fig. 4. (a) RMS-amplitude of relative sensor motion $\Delta x_{\mathrm{bpf}}[n]$ during rest (dots) and walking (circles). (b) RMS-amplitude of head motion $a_{v\_\mathrm{bpf}}[n]$ during rest and walking. (c) Mean (open triangle) and SD (filled triangle) of FLL-frequency time-derivative $df_{\mathrm{FLL}}[n]$ during walking for $\Delta x[n]$. (d) Mean and SD of $df_{\mathrm{FLL}}[n]$ during walking for $a_v[n]$. (e) Mean and SD of gating function $G[n]$ during walking for $\Delta x[n]$. (f) Mean and SD of $G[n]$ during walking for $a_v[n]$. bpf: band-pass filtered; FLL: frequency-locked loop; RMS: root mean square; SD: standard deviation.

obtained via head motion $a_v[n]$. Subtracting $ma_{\mathrm{est}}[n]$ from $ppg_{\mathrm{bpf}}[n]$ gave the stable-amplitude artifact-reduced signal $ppg_{\mathrm{ar}}[n]$ in Fig. 5c. Fig. 5d and e respectively show that the IBIs and SpO_2 derived from the motion-affected signals varied periodically (diamonds). The IBIs and SpO_2 after artifact reduction (squares) did not show this variation any longer, and were closer to the ECG-derived IBIs (crosses in Fig. 5d) and commercial device SpO_2 (crosses in Fig. 5e), respectively. The exclusion of pulses with too small pulsatility (24) caused the gaps in the IBIs and SpO_2 before artifact reduction. After artifact reduction, no pulses were excluded in Figs. 5d and e.

The spectrograms in Fig. 6 further illustrate the effect of walking and artifact reduction. Fig. 6a shows that step-rate related frequency components appear in $ppg_{\mathrm{bpf}}[n]$ during walking in addition to the PR related frequency components. The component at half the step rate was due to guiding the sensor wire behind the left ear, causing pulling of the sensor each time the head turned right. Fig. 6b shows that $ma_{\mathrm{est}}[n]$ captured all step-rate related components, with slight leakage of PR related components. Fig. 6c shows that subtracting $ma_{\mathrm{est}}[n]$ from $ppg_{\mathrm{bpf}}[n]$ effectively removed the artifacts.

Fig. 7 shows the effect of artifact reduction on pulse detection. It shows the percentage p_{A_rd} of candidate pulses in the red PPG signal which was associated with an R-peak before artifact reduction (diamonds), and after artifact reduction using $\Delta x[n]$ (triangles) and $a_v[n]$ (squares). For subject 1 at 5 and 6 km/h, subject 2 at all speeds, and subject 6 at 6-8 km/h, artifact reduction increased p_{A_rd} because the algorithm removed destructive interference by the artifact, so more pulses exceeded plt_{thr}. This effect is illustrated in Fig. 5. For subject 4 at all speeds, artifact reduction decreased p_{A_rd} because the algorithm partly removed cardiac pulses with a PR close to the step rate, so less pulses exceeded plt_{thr}. For subject 4 at 4-6 km/h, the decrease in p_{A_rd} was smaller for $\Delta x[n]$ than for $a_v[n]$, because $G[n]$ was less active for $\Delta x[n]$ than for $a_v[n]$ (Fig. 4e and f). For subject 1 at 4 km/h, subjects 3 and 5 at all speeds, and subject 6 at 4 km/h, artifact reduction affected p_{A_rd} little, because destructive interference was not pronounced, and step rate and PR were distinct. For subject 1 at 7 and 8 km/h, and subject 6 at 5 km/h, artifact

TABLE I
EVALUATION OF RELATIVE SENSOR MOTION Δx AND HEAD MOTION a_v.

	Measure	Subject 1	Subject 2	Subject 3	Subject 4	Subject 5	Subject 6	Average
Δx	RMS Δx_{bpf} walking/rest [-]	10.9±4.4	7.8±4.3	4.2±0.5	4.6±2.3	3.9±1.4	4.0±1.6	5.9±3.7
	SD f_{FLL} [min^{-1}]	1.3±0.1	10.5±12.6	29.7±5.5	23.4±11.7	16.4±11.3	19.6±9.7	16.8±12.7
a_v	RMS a_{v_bpf} walking/rest [-]	119.9±36.6	166.2±57.0	66.5±25.3	56.1±10.0	35.6±18.7	48.2±18.6	82.1±55.0
	SD f_{FLL} [min^{-1}]	1.2±0.1	1.4±0.6	4.7±1.9	2.0±1.4	1.7±0.7	2.7±1.1	2.3±1.6

Results in mean ± standard deviation. RMS walking/rest: ratio of the root mean square amplitudes during walking and rest; SD f_{FLL}: standard deviation of the frequency tracked by the frequency-locked loop after the initial 10 s transient.

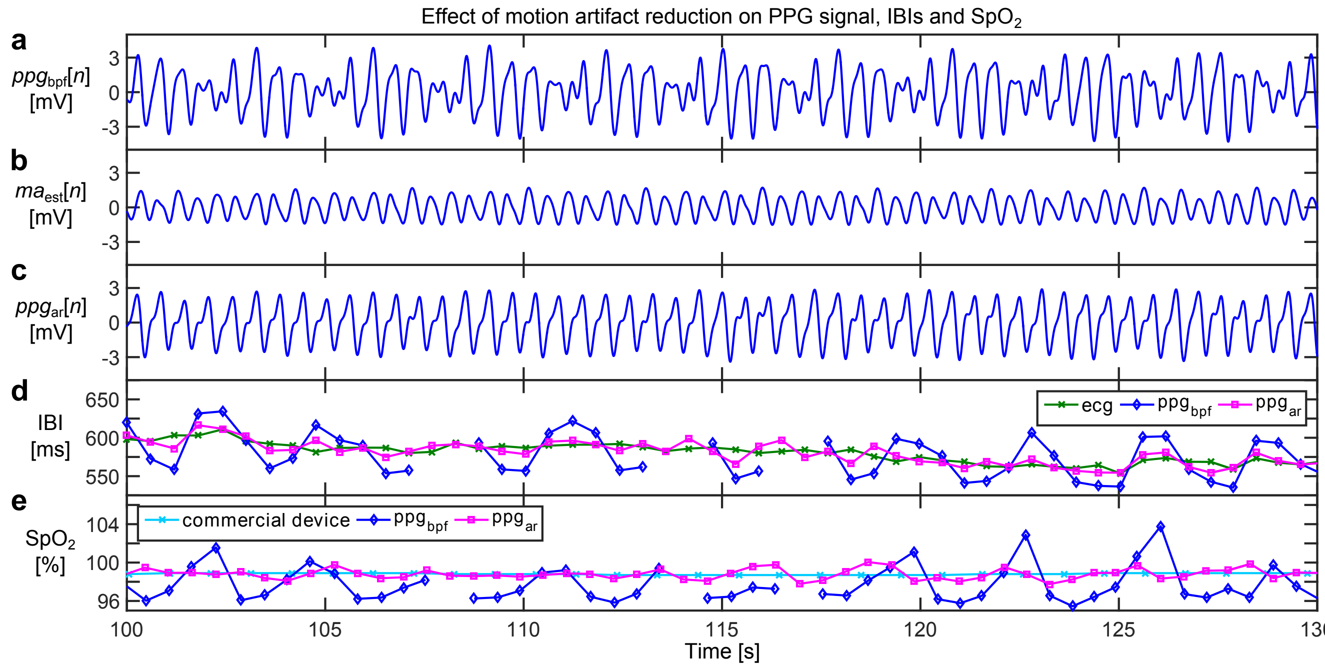

Fig. 5. Example time-traces of the infrared PPG signal, IBIs, and SpO_2 from subject 6 while walking at 6 km/h. (a) Walking causes periodic variation in $ppg_{\mathrm{bpf}}[n]$. (b) Motion artifact estimate $ma_{\mathrm{est}}[n]$ obtained via head motion $a_v[n]$. (c) Artifact-reduced signal $ppg_{\mathrm{ar}}[n] = ppg_{\mathrm{bpf}}[n] - ma_{\mathrm{est}}[n]$. (d) IBIs from $ppg_{\mathrm{bpf}}[n]$ vary periodically (diamonds). IBIs from $ppg_{\mathrm{ar}}[n]$ (squares) are closer to ECG RRIs (crosses). (e) SpO_2 from $ppg_{\mathrm{bpf}}[n]$ varies periodically (diamonds). SpO_2 from $ppg_{\mathrm{ar}}[n]$ (squares) is closer to commercial device SpO_2 (crosses). Gaps in IBIs and SpO_2 for $ppg_{\mathrm{bpf}}[n]$ are excluded pulses with too small pulsatility. ECG: electrocardiography; IBI: inter-beat interval; PPG: photoplethysmography; RRI: R-peak to R-peak interval; SpO_2: oxygen saturation.

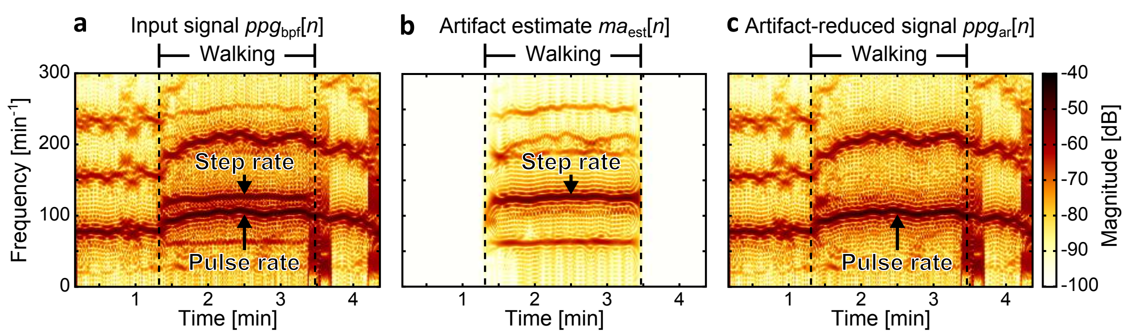

Fig. 6. Example spectrograms of the infrared PPG signal from subject 6 while walking at 6 km/h. (a) The measured PPG signal $ppg_{\mathrm{bpf}}[n]$ contains artifacts at step-rate related frequencies during walking. (b) The artifact estimate $ma_{\mathrm{est}}[n]$ contains all step-rate related frequency components. (c) Subtracting $ma_{\mathrm{est}}[n]$ from $ppg_{\mathrm{bpf}}[n]$ effectively removes the motion artifacts in $ppg_{\mathrm{ar}}[n]$. PPG: photoplethysmography.

reduction affected p_{A_rd} little, because the improvement by removal of destructive interference balanced the deterioration due to comparable step rate and PR. For subject 6 at 4 and 5 km/h, spurious detection of dicrotic notches lowered p_{A_rd} overall. Results were similar for the IR PPG signal.

Fig. 8 gives an overview of ΔIBI for PPG signals at rest (R), with motion artifacts (M), and after artifact reduction using $\Delta x[n]$ and $a_v[n]$. The middle line is the median, the box extends from the 25^{th} to the 75^{th} percentile, and the whiskers from the 10^{th} to the 90^{th} percentile. Motion artifacts increased the spread in ΔIBI to various degrees. Motion hardly affected ΔIBI for subject 4, because step rate and PR were comparable. The percentages with Δx and a_v in Fig. 8 are the changes in the 10^{th} to the 90^{th} percentile range after artifact reduction compared to M. The numbers with Δx and a_v in Fig. 8 are the 10^{th} to the 90^{th} percentile ranges after artifact reduction divided by this range at R. Table II gives the averages. Artifact reduction reduced the spread in ΔIBI for subjects 1 and 2. For subject 1, artifact reduction was less at 7 and 8 km/h compared to 4-6 km/h, because step rate and PR partly coincided. For subject 2, a less active $G[n]$ for $\Delta x[n]$ at 4 and 8 km/h affected artifact reduction compared to 5-7 km/h (Fig. 4e). For subject 3, using $\Delta x[n]$ reduced ΔIBI by at most 15% at 6 km/h. The poor quality of $\Delta x[n]$ hampered tracking of the step rate, as shown by $df_{\mathrm{FLL}}[n]$ and $G[n]$ in Fig. 4c and e, respectively. Using $a_v[n]$ only improved ΔIBI at 6-8 km/h. The larger step-rate variation of subject 3 presumably affected the artifact reduction (Table I). For subject 4 at 4-6 km/h, ΔIBI increased after artifact reduction, because of coinciding step rate and PR. At 7 and 8 km/h, some reduction in ΔIBI was achieved, because step rate and PR coincided less during walking. For subjects 5 and 6, reduction in ΔIBI

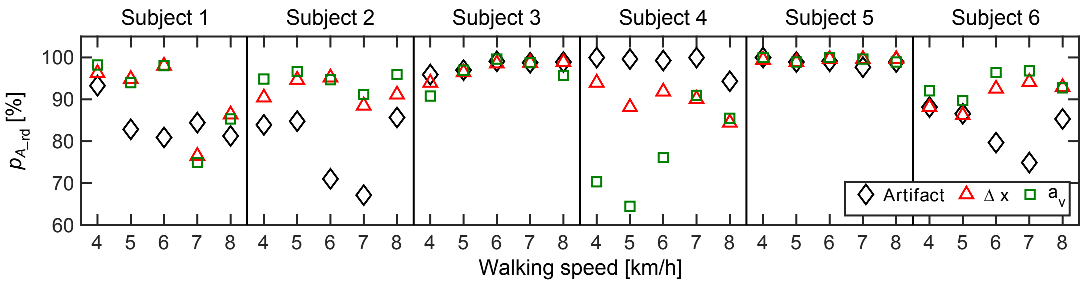

Fig. 7. Percentage of candidate pulses in the red PPG signal which is associated with an R-peak. The percentages were determined in the walking intervals before artifact reduction (diamonds), and after artifact reduction using relative sensor motion $\Delta x[n]$ (triangles) and head motion $a_v[n]$ (squares). Results were similar for the infrared PPG signal. PPG: photoplethysmography.

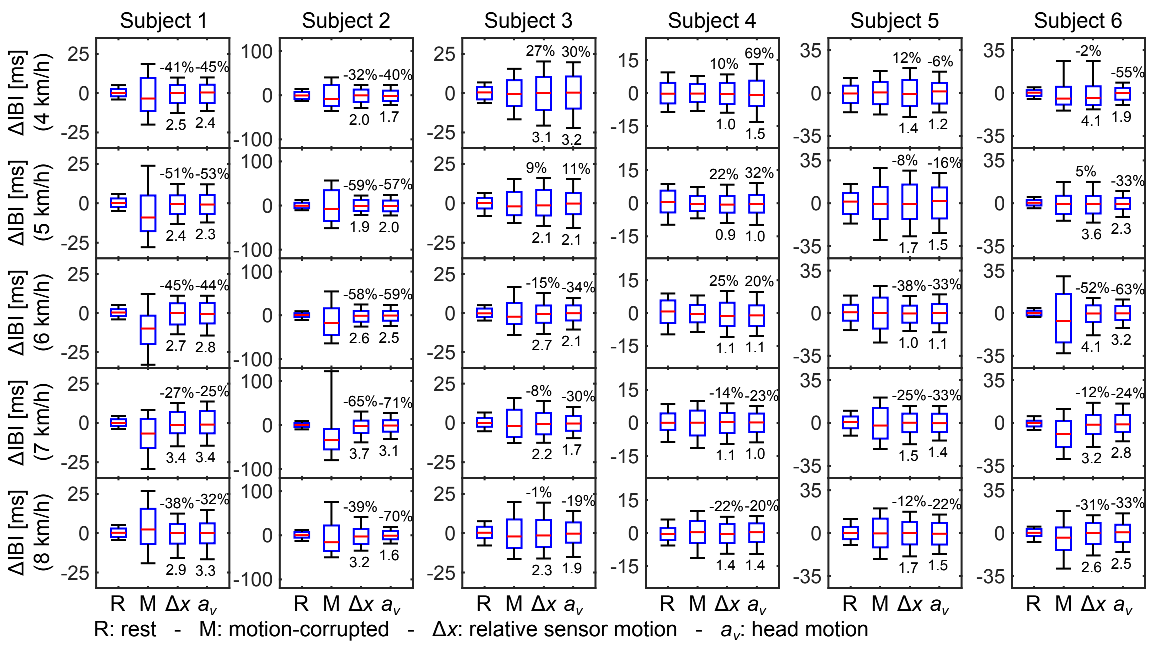

Fig. 8. ΔIBIs from infrared PPG signals at rest (R), with motion artifacts (M), and after artifact reduction using relative sensor motion (Δx) and head motion (a_v). From top to bottom, walking speed increases from 4 to 8 km/h. The middle line is the median, the box extends from the 25^{th} to the 75^{th} percentile, and the whiskers from the 10^{th} to the 90^{th} percentile. The percentages with Δx and a_v are the changes in the whisker range after artifact reduction compared to this range at M. The numbers with Δx and a_v are the ratios of the whisker ranges after artifact reduction and at R. IBI = inter-beat interval; PPG: photoplethysmography.

was achieved at 6-8 km/h for $\Delta x[n]$, and at all speeds for $a_v[n]$. At 4 and 5 km/h, improvement in ΔIBI was affected by a poor quality of $\Delta x[n]$, which hampered tracking of the step rate, as shown by $df_{\mathrm{FLL}}[n]$ and $G[n]$ in Fig. 4c and e, respectively. The 10^{th} to 90^{th} percentile range of ΔIBI after artifact reduction was mostly 1 to 3 times this range at rest.

Fig. 9 gives an overview of the spread in SpO_2 measured by the commercial device during rest (C), and derived from the PPG signals at rest (R), with motion artifacts (M), and after artifact reduction (Δx and a_v). The ranges and numbers shown in Fig. 9 are obtained in the same way as in Fig. 8. Table II gives the averages. For subject 2, the 10^{th} to 90^{th} percentile range of SpO_2 was about 4-5% at rest, whereas this was about 1-2% for the other subjects. This was caused by the lower SNR of the PPG signals of subject 2. Motion increased the spread in SpO_2 to various degrees. Artifact reduction decreased the spread in SpO_2 for subjects 1 and 2. For subject 1, step rate and PR partly coincided at 7 and 8 km/h, but only at 8 km/h artifact reduction was affected. For subject 2, a less active $G[n]$ for $\Delta x[n]$ at 4 and 8 km/h affected artifact reduction compared to 5-7 km/h (Fig. 4e). For subject 3, spread in SpO_2 was only slightly reduced at 6 and 7 km/h for $\Delta x[n]$. The poor quality of $\Delta x[n]$ hampered tracking of the step rate, as shown by $df_{\mathrm{FLL}}[n]$ and $G[n]$ in Fig. 4c and e, respectively. For $a_v[n]$, a relatively small reduction in spread in SpO_2 was achieved at 4-7 km/h. The irregular step rate of subject 3 presumably affected the reduction in spread in SpO_2 (Table I). For subject 4 at 4-6 km/h, the coinciding step rate and PR hampered artifact reduction for $\Delta x[n]$ and $a_v[n]$. At 7 and 8 km/h, some reduction in spread in SpO_2 was achieved, because step rate and PR coincided less during walking. For subjects 5 and 6, reduction in spread in SpO_2 was achieved at 6-8 km/h for $\Delta x[n]$, and at all speeds for $a_v[n]$. At 4 and 5 km/h, reduction of spread in SpO_2 was affected by a poor quality of $\Delta x[n]$, which hampered tracking of the step rate, as shown by $df_{\mathrm{FLL}}[n]$ and $G[n]$ in Fig. 4c and e, respectively. The

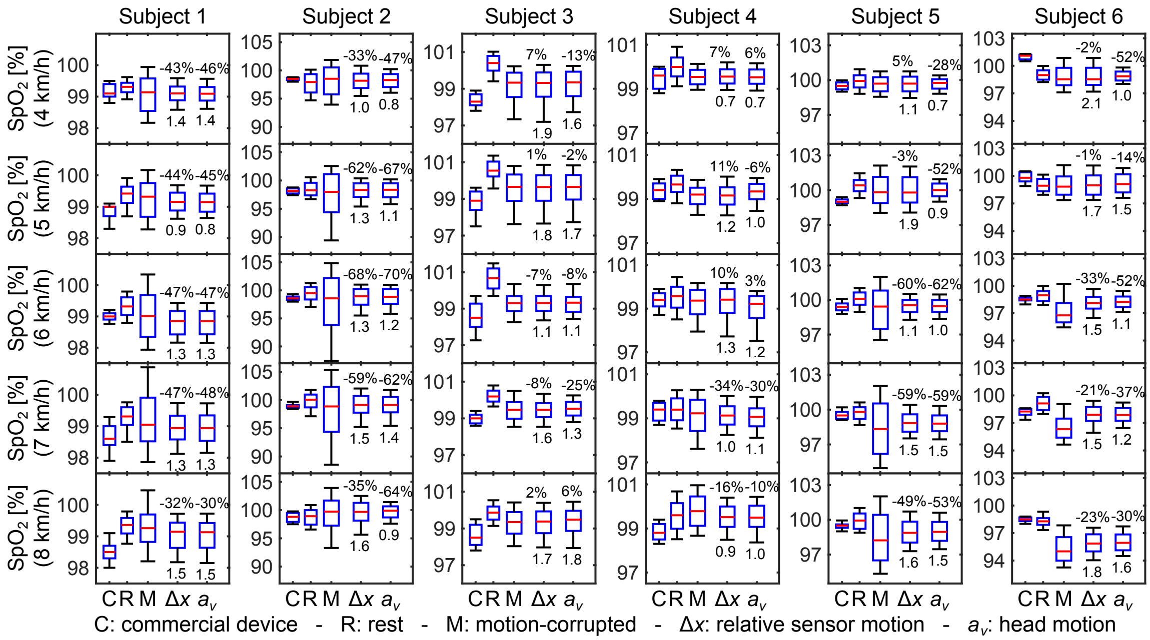

Fig. 9. SpO_2 from the commercial device at rest (C), and from red and infrared PPG signals at rest (R), with motion artifacts (M), and after artifact reduction using relative sensor motion (Δx) and head motion (a_v). From top to bottom, walking speed increases from 4 to 8 km/h. The middle line is the median, the box extends from the 25^{th} to the 75^{th} percentile, and the whiskers from the 10^{th} to the 90^{th} percentile. The percentages with Δx and a_v are the changes in the whisker range after artifact reduction compared to this range at M. The numbers with Δx and a_v are the ratios of the whisker ranges after artifact reduction and at R. PPG: photoplethysmography; SpO_2: oxygen saturation.

10^{th} to 90^{th} percentile range of SpO_2 after artifact reduction was mostly 1 to 2 times the range at rest. The median SpO_2 obtained via (26) at rest and after artifact reduction did not differ more than 2.6% from the median SpO_2 measured by the commercial device at rest.

VI. Discussion

We developed a generic algorithm to remove periodic motion artifacts from PPG signals (Fig. 2). The algorithm recovered an artifact-reduced PPG signal for further time-domain beat-to-beat analysis in addition to, e.g., spectral analysis. We described the motion artifact using a quadrature basis so only two coefficients are needed per frequency component and the artifact estimate contains no undesired frequency-shifted components [30], [31]. These advantages are not offered by approaches directly estimating FIR filter coefficients [30], [31]. We retrospectively evaluated the algorithm on forehead PPG signals measured while walking on a treadmill (Fig. 1a). As motion references we compared sensor motion relative to the skin, $\Delta x[n]$, measured via SMI, and head motion, $a_v[n]$, measured with an accelerometer (Fig. 1b). We used a SOGI-based structure with an FLL to track the step rate in the reference signals (Fig. 3). We showed that $a_v[n]$ had a better SNR than $\Delta x[n]$, and that the FLL tracked the step rate more consistently in $a_v[n]$ than in $\Delta x[n]$ (Fig. 4 and Table I). Therefore, $a_v[n]$ outperformed $\Delta x[n]$ as motion reference. The FLL frequency was used in a quadrature harmonic model to describe the motion artifact (14). An LMS algorithm estimated the amplitudes of the quadrature components. Subtracting the artifact estimate from the measured PPG signal effectively reduced the artifact in the resulting artifact-reduced PPG signal (Figs. 5 and 6). When the step rate was stable and different than the PR, the proposed algorithm reduced ΔIBI and the spread in SpO_2 by 30-70% (Figs. 8 and 9, and Table II). When step rate and PR were comparable, the algorithm partly removed cardiac pulses too. This was detected by thresholding

TABLE II
Evaluation of motion artifact reduction using relative sensor motion Δx and head motion a_v.

	Measure	Subject 1	Subject 2	Subject 3	Subject 4	Subject 5	Subject 6	Average
Δx	ΔIBI 10-90 perc. [%]	-40±9	-51±14	2±16	4±21	-14±19	-18±23	-20±26
	ΔIBI vs rest [-]	2.8±0.4	2.6±0.8	2.5±0.4	1.1±0.2	1.5±0.3	3.5±0.7	2.3±0.9
	SpO_2 10-90 perc. [%]	-42±6	-52±16	-1±7	-5±20	-33±32	-16±14	-25±25
	SpO_2 vs rest [-]	1.3±0.2	1.3±0.2	1.6±0.3	1.0±0.2	1.4±0.3	1.7±0.2	1.4±0.3
a_v	ΔIBI 10-90 perc. [%]	-40±11	-59±13	-9±28	16±38	-22±11	-42±16	-26±32
	ΔIBI vs rest [-]	2.8±0.5	2.2±0.6	2.2±0.6	1.2±0.2	1.3±0.2	2.5±0.5	2.0±0.7
	SpO_2 10-90 perc. [%]	-43±7	-62±9	-9±12	-8±14	-51±14	-37±16	-35±24
	SpO_2 vs rest [-]	1.2±0.3	1.1±0.2	1.5±0.3	1.0±0.2	1.1±0.3	1.3±0.3	1.2±0.3

Results in mean ± standard deviation. ΔIBI / SpO_2 10-90 perc.: reduction in 10^{th} to 90^{th} percentile range of the IBI error / spread in SpO_2 achieved by artifact reduction; ΔIBI / SpO_2 vs rest: 10^{th} to 90^{th} percentile range of the IBI error / spread in SpO_2 after artifact reduction relative to this range at rest; IBI: inter-beat interval; SpO_2: oxygen saturation.

the magnitude of the baseline-normalized pulses in the artifact-reduced PPG signal, to exclude too small pulses for further analysis (Fig. 7).

Degradation of the algorithm performance occurred in three occasions. Motion artifacts were removed to a lesser extent, when a low-quality motion reference signal hampered tracking of the step rate, or when the step rate varied faster than the algorithm could track. Cardiac pulses were partly removed when step rate and PR were comparable. However, when the step rate was stable and distinct from the PR, and the motion reference signal consistently contained a component at the step rate, the proposed algorithm considerably reduced ΔIBI and the spread in SpO_2. Therefore, the proposed algorithm can facilitate analysis of IBIs and SpO_2 during periodic motion in, e.g., ADL, sports, CPX, or CPR. Coinciding motion frequency and PR can furthermore be identified when pulses in the artifact-reduced PPG signal become too small.

The relative sensor motion $\Delta x[n]$ was not a stable motion reference signal. The FLL did not steadily track the step rate in $\Delta x[n]$ in 14 out of 30 measurements (Fig. 4). This may indicate little relative sensor motion in these cases. Insufficient optical feedback into the LD may also contribute to a poor signal quality of $\Delta x[n]$. Therefore, we recommend using an accelerometer as a motion reference for (quasi-)periodic motion.

After successful artifact reduction, the spread in ΔIBI was larger compared to measurements at rest (Fig. 8 and Table II). This may result from residual motion artifacts, or from physiological fluctuations in IBIs during walking caused by variations in pre-ejection time and pulse transit time [22]. Inaccuracies in the ECG signal during walking may also contribute, resulting from electrode-skin motion, and the electromyogram [58].

The spread in SpO_2 after artifact reduction was about 1 to 2 times the spread at rest, and was therefore smaller than the spread in ΔIBI after artifact reduction, which was about 1 to 3 times the spread at rest (Figs. 8 and 9, and Table II). This is presumably caused by the different nature of the performance measures. We only considered the spread in SpO_2 without direct comparison to a reference, and we therefore do not have a measure of the SpO_2 accuracy. In contrast, ΔIBI was a beat-to-beat comparison of IBIs and ECG-derived RRIs. Consequently, although the spread in SpO_2 after artifact reduction is more comparable to the spread at rest, this does not indicate a better performance for SpO_2 than for IBIs.

The proposed solution has some limitations. The algorithm can only deal with slowly-varying periodic motion artifacts. When the motion frequency and PR coincide, no improvement can be obtained. In a real-world application, an additional algorithm may be required which first assesses presence and periodicity of motion to determine whether the proposed algorithm should be initiated. Furthermore, a limited number of measurements have been performed on a limited number of subjects, resulting in only a preliminary validation of the algorithm. Also, the periodic motion artifacts generated on the treadmill may be more periodic than encountered in ADL. SpO_2 accuracy has not been assessed. Only the variation in SpO_2 has been quantified, assuming a relatively constant SpO_2 for healthy subjects.

VII. Conclusions

The proposed generic algorithm can effectively remove periodic motion artifacts from PPG signals measured while walking on a treadmill. A SOGI-based structure with an FLL can track the step rate in a motion reference signal. An accelerometry-derived motion reference signal outperforms an SMI-derived motion reference signal, which measures sensor motion relative to the skin. Periodic motion artifacts can be described by a harmonic model of quadrature components with frequencies related to the tracked step rate. Subtracting the harmonic model from the measured PPG signal effectively removes the motion artifacts. More stable IBI and SpO_2 measurements can be derived from the resulting artifact-reduced PPG signals if the step rate and PR are distinct. If step rate and PR are comparable, also cardiac pulses are partly removed, which can be detected by thresholding the magnitude of the baseline-normalized pulses in the artifact-reduced PPG signal.

Acknowledgements

This work was supported by NL Agency, IOP Photonic Devices, IPD083359 HIP, Hemodynamics by Interferometric Photonics. We thank Dr J. Veen from the HAN University of Applied Sciences, Dr A. van der Lee, Dr P. Woerlee, Dr W. Peeters and Dr J. Mühlsteff from Philips Research, and Prof J. Bergmans from the Eindhoven University of Technology for the valuable discussions, and Mr B. Wassink from VDL ETG Research bv for customizing the forehead sensor.

References

[1] J. Allen, "Photoplethysmography and its application in clinical physiological measurement," *Physiol. Meas.*, vol. 28, no. 3, pp. R1–39, Mar. 2007.

[2] A. Reisner, P.A. Shaltis, D. McCombie, and H.H. Asada, "Utility of the photoplethysmogram in circulatory monitoring," *Anesthesiology*, vol. 108, no. 5, pp. 950–58, May 2008.

[3] R. Sahni, "Noninvasive monitoring by photoplethysmography," *Clin. Perinatol.*, vol. 39, no. 3, pp. 573–83, Sep. 2012.

[4] P. S. Addison, J. N. Watson, M. L. Mestek, J. P. Ochs, A. A. Uribe, and S. D. Bergese, "Pulse oximetry-derived respiratory rate in general care floor patients," *J. Clin. Monit. Comput.*, vol. 29, no. 1, pp. 113–20, Feb. 2015.

[5] T. Tamura, Y. Maeda, M. Sekine, and M. Yoshida, "Wearable photoplethysmographic sensors - past and present," *Electronics*, vol. 3, no. 2, pp. 282–302, Apr. 2014.

[6] A. B. Hertzman "The blood supply of various skin areas as estimated by the photoelectric plethysmograph," *Am. J. Physiol.*, vol. 124, no. 2, pp. 328–40, July 1938.

[7] Y. Mendelson, "Pulse oximetry: theory and applications for noninvasive monitoring," *Clin. Chem.*, vol. 38, no. 9, pp. 1601–7, Sep. 1992.

[8] K. Nakajima, T. Tamura, and H. Miike, "Monitoring of heart and respiratory rates by photoplethysmography using a digital filtering technique," *Med. Eng. Phys.*, vol. 18, no. 5, pp. 365–72, Jul. 1996.

[9] T.L. Rusch, R. Sankar, and J. E. Scharf, "Signal processing methods for pulse oximetry," *Comput. Biol. Med.*, vol. 26, no. 2, pp. 143–59, Mar. 1996.

[10] J. A. Pologe, "Pulse oximetry: technical aspects of machine design," *Int. Anesthesiol. Clin.*, vol. 25, no. 3, pp. 137–53, Feb. 1987.

[11] J. G. Webster, Ed., *Design of pulse oximeters*(*Medical Science Series*). New York, NY, USA: Taylor & Francis Group, 1997.

[12] T. Aoyagi, "Pulse oximetry: its invention, theory, and future," *J. Anesth.*, vol. 17, no. 4, pp. 259–66, Jan. 2003.

[13] P. D. Mannheimer, "The light-tissue interaction of pulse oximetry," *Anesth. Analg.*, vol. 105, no. 6 Suppl, pp. S10–7, Dec. 2007.

[14] M. Nitzan, A. Romem, and R. Koppel, "Pulse oximetry: fundamentals and technology update," *Med. Devices (Auckl).*, vol. 7, pp. 231–9, Jul. 2014.

[15] H. H. Asada, P. Shaltis, A. Reisner, S. Rhee, and R. C. Hutchinson, "Mobile monitoring with wearable photoplethysmographic biosensors," *IEEE Trans. Biomed. Eng.*, vol. 22, no. 3, pp. 28–40, July 2003.

[16] G. J. Balady, R. Arena, K. Sietsema, J. Myers, L. Coke, G. F. Fletcher, D. Forman, B. Franklin, M. Guazzi, M. Gulati, S. J. Keteyian, C. J. Lavie, R. Macko, D. Mancini, and R. V. Milani, "Clinician's Guide to cardiopulmonary exercise testing in adults: a scientific statement from the American Heart Association," *Circulation*, vol. 122, no. 2, pp. 191–225, July 2010.

[17] D. E. Forman, J. Myers, C. J. Lavie, M. Guazzi, B. Celli, and R. Arena, "Cardiopulmonary exercise testing: relevant but underused," *Postgrad. Med.*, vol. 122, no. 6, pp. 68–86, Nov. 2010.

[18] R.W.C.G.R. Wijshoff, T. van der Sar, P.H. Peeters, R. Bezemer, P. Aelen, I.W.F. Paulussen, S.C.M.A. Ordelman, A. Venema, P.F.J. van Berkom, R.M. Aarts, P.H. Woerlee, G.-J. Scheffer, and G.J. Noordergraaf, "Detection of a spontaneous pulse in photoplethysmograms during automated cardiopulmonary resuscitation in a porcine model," *Resuscitation*, vol. 84, no. 11, pp. 1625–1632, Nov. 2013.

[19] R. W. C. G. R. Wijshoff, A. M. T. M. Asten, W. H. Peeters, R. Bezemer, G. J. Noordergraaf, M. Mischi, and R. M. Aarts, "Photoplethysmography-based algorithm for detection of cardiogenic output during cardiopulmonary resuscitation," *IEEE Trans. Biomed. Eng.*, vol. 62, no. 3, pp. 909–921, March 2015.

[20] J. Van Andel, C. Ungureanu, R. Aarts, F. Leijten, and J. Arends, "Using photoplethysmography in heart rate monitoring of patients with epilepsy," *Epilepsy Behav.*, vol. 45, no. 4, pp. 142–145, Apr. 2015.

[21] W.J.C. Van Elmpt, T.M.E. Nijsen, P.A.M. Griep, and J.B.A.M. Arends, "A model of heart rate changes to detect seizures in severe epilepsy," *Seizure*, vol. 15, no. 6, pp. 366–375, June 2006.

[22] A. Schäfer, and J. Vagedes, "How accurate is pulse rate variability as an estimate of heart rate variability? A review on studies comparing photoplethysmographic technology with an electrocardiogram," *Int. J. Cardiol.* vol. 166, no. 1, pp. 15–29, June 2013.

[23] L. Ferranti, and R. Laureanti, "Atrial fibrillation detection in PPG signal recorded through a wristband device," M.S. thesis, Dept. of Electronics, Information and Bioengineering, Politecnico di Milano, Milan, Italy, Dec. 2015.

[24] G. Comtois, Y. Mendelson, and P. Ramuka, "A comparative evaluation of adaptive noise cancellation algorithms for minimizing motion artifacts in a forehead-mounted wearable pulse oximeter," *Conf. Proc. IEEE Eng. Med. Biol. Soc.*, pp. 1528–31, Aug. 2007.

[25] P. T. Gibbs, and H. H. Asada, "Reducing motion artifact in wearable bio-sensors using MEMS accelerometers for active noise cancellation," *Proc. of the American Control Conf.*, vol. 3, pp. 1581–6, June 2005.

[26] L. B. Wood, and H. H. Asada, "Low variance adaptive filter for cancelling motion artifact in wearable photoplethysmogram sensor signals," *Conf. Proc. IEEE Eng. Med. Biol. Soc.*, pp. 652–5, Aug. 2007.

[27] B. Lee, J. Han, H. J. Baek, J. H. Shin, K. S. Park, and W. J. Yi, "Improved elimination of motion artifacts from a photoplethysmographic signal using a Kalman smoother with simultaneous accelerometry," *Physiol. Meas.*, vol. 31, no. 12, pp. 1585–603, Dec. 2010.

[28] M.-Z. Poh, N. C. Swenson, and R. W. Picard "Motion-tolerant magnetic earring sensor and wireless earpiece for wearable photoplethysmography," *IEEE Trans. Inf. Technol. Biomed.*, vol. 14, no. 3, pp. 786–94, Feb. 2010.

[29] H. Han, and J. Kim, "Artifacts in wearable photoplethysmographs during daily life motions and their reduction with least mean square based active noise cancellation method," *Comput. Biol. Med.*, vol. 42, no. 4, pp. 387–93, Apr. 2012.

[30] B. Widrow, J.R. Glover, J.M. McCool, J. Kaunitz, C.S. Williams, R.H. Hearn, J.R. Zeidler, E. Dong, JR., and R.C. Goodlin, "Adaptive noise cancelling: principles and applications," *Proc. IEEE*, vol. 63, no. 12, pp. 105–12, Dec. 1975.

[31] J.R. Glover JR, "Adaptive noise cancelling applied to sinusoidal interferences,", *IEEE Trans. Acoust., Speech, Signal Processing*, vol. ASSP–25, no. 6, pp. 484–91, Dec. 1977.

[32] M. J. Hayes and P. R. Smith, "Artifact reduction in photoplethysmography," *Appl. Opt.*, vol. 37, no. 31, pp. 7437–46, Nov. 1998.

[33] M.J. Hayes, and P.R. Smith, "A new method for pulse oximetry possessing inherent insensitivity to artifact," *IEEE Trans. Biomed. Eng.*, vol. 48, no. 4, pp. 452–61, Apr. 2001.

[34] J. A. C. Patterson, and G.-Z. Yang, "Ratiometric artifact reduction in low power reflective photoplethysmography," *IEEE Trans. Biomed. Circuits Syst.*, vol. 5, no. 4, pp. 330–8, July 2011.

[35] F. M. Coetzee, and Z. Elghazzawi, "Noise-resistant pulse oximetry using a synthetic reference signal," *IEEE Trans. Biomed. Eng.*, vol. 47, no. 8, pp. 1018–26, Aug. 2000.

[36] M. R. Ram, K. V. Madhav, E. H. Krishna, N. R. Komalla, and K. A. Reddy, "A novel approach for motion artifact reduction in PPG signals based on AS-LMS adaptive filter," *IEEE Trans. Instrum. Meas.*, vol. 61, no. 5, pp. 1445–57, May 2012.

[37] R. Yousefi, M. Nourani, S. Ostadabbas, and I. Panahi, "A motion-tolerant adaptive algorithm for wearable photoplethysmographic biosensors," *IEEE J. Biomed. Health Inform.*, vol. 18, no. 2, pp. 670–81, Mar. 2014.

[38] B. S. Kim, and S. K. Yoo, "Motion artifact reduction in photoplethysmography using independent component analysis," *IEEE Trans. Biomed. Eng.*, vol. 53, no. 3, pp. 566–8, Mar. 2006.

[39] R. Krishnan, B. Natarajan, and S. Warren, "Two-stage approach for detection and reduction of motion artifacts in photoplethysmographic data," *IEEE Trans. Biomed. Eng.*, vol. 57, no. 8, pp. 1867–76, Aug. 2010.

[40] H.-W. Lee, J.-W. Lee, W.-G. Jung, and G.-K. Lee, "The periodic moving average filter for removing motion artifacts from PPG signals," *Int. J. Control Autom.*, vol. 5, no. 6, pp. 701–6, Dec. 2007.

[41] H. Fukushima, H. Kawanaka, M. S. Bhuiyan, and K. Oguri, "Estimating heart rate using wrist-type Photoplethysmography and acceleration sensor while running," *Conf. Proc. IEEE Eng. Med. Biol. Soc.*, pp. 2901–4, Aug. 2012.

[42] Z. Zhang, Z. Pi, and B. Liu, "TROIKA: A general framework for heart rate monitoring using wrist-type photoplethysmographic signals during intensive physical exercise," *IEEE Trans. Biomed. Eng.*, vol. 62, no. 2, pp. 522–31, Feb. 2015.

[43] Z. Zhang, "Photoplethysmography-based heart rate monitoring in physical activities via joint sparse spectrum reconstruction," *IEEE Trans. Biomed. Eng.*, vol. 62, no. 8, pp. 1902–10, Aug. 2015.

[44] S.M.A. Salehizadeh, D. Dao, J. Bolkhovsky, C. Cho, Y. Mendelson, and K.H. Chon, "A novel time-varying spectral filtering algorithm for reconstruction of motion artifact corrupted heart rate signals during intense physical activities using a wearable photoplethysmogram sensor," *Sensors*, vol. 16, no. 10, pp. 1–20, Dec. 2015.

[45] L. Wang, B. P. L. Lo, and G.-Z. Yang, "Multichannel reflective PPG earpiece sensor with passive motion cancellation," *IEEE Trans. Biomed. Circuits Syst.*, vol. 1, no. 4, pp. 235–41, Dec. 2007.

[46] J. M. Goldman, M. T. Petterson, R. J. Kopotic, and S. J. Barker, "Masimo signal extraction pulse oximetry," *J. Clin. Monit. Comput.*, vol. 16, no. 7, pp. 475–83, Jan. 2000.

[47] Y.-S. Yan, and Y.-T. Zhang, "An efficient motion-resistant method for wearable pulse oximeter," *IEEE T. Inf. Technol. B.*, vol. 12, no. 3, pp. 399–405, May 2008.

[48] Y.-S. Yan, C. C. Poon, and Y.-T. Zhang, "Reduction of motion artifact in pulse oximetry by smoothed pseudo Wigner-Ville distribution," *J. Neuroeng. Rehabil.*, vol. 2, no. 1, p. 3, Mar. 2005.

[49] P. Rodríguez, A Luna, I Candela, R Mujal, R Teodorescu, and F Blaabjerg, "Multiresonant frequency-locked loop for grid synchronization of power converters under distorted grid conditions," *IEEE Trans. Ind. Electron.*, vol. 58, no. 1, pp. 127–38, Jan. 2011.

[50] R. W. C. G. R. Wijshoff, J. Veen, A. M. Van der Lee, L. Mulder, J.M.A. Stijnen, S. Van Tuijl, and R. M. Aarts, "PPG motion artifact handling using a self-mixing interferometric sensor," *Proc. SPIE*, vol. 7894, pp. 0F1–13, Jan. 2011.

[51] R. W. C. G. R. Wijshoff, M. Mischi, J. Veen, A. M. Van der Lee, and R. M. Aarts, "Reducing motion artifacts in photoplethysmograms by using relative sensor motion: phantom study," *J. Biomed. Opt.*, vol. 17, no. 11, pp. 117007–1–15, Nov. 2012.

[52] R. W. C. G. R. Wijshoff, M. Mischi, P. H. Woerlee, and R. M. Aarts, "Improving pulse oximetry accuracy by removing motion artifacts from photoplethysmograms using relative sensor motion: a preliminary study," in *Oxygen Transport to Tissue XXXV* (*Advances in Experimental Medicine and Biology* vol 789), S. Van Huffel, G. Naelaers, A. Caicedo, D. F. Bruley, and D. K. Harrison, Eds., New York, NY, USA: Springer Science+Business Media, 2013, pp. 411–7.

[53] Y. Mendelson, and B. D. Ochs, "Noninvasive pulse oximetry utilizing skin reflectance photoplethysmography," *IEEE Trans. Biomed. Eng.*, vol. 35, no. 10, pp. 798–805, Oct. 1988.

[54] R. G. Haahr, S. B. Duun, M. H. Toft, B. Belhage, J. Larsen, K. Birkelund, and E. V. Thomsen, "An electronic patch for wearable health monitoring by reflectance pulse oximetry," *IEEE Trans. Biomed. Circuits Syst.*, vol. 6, no. 1, pp. 45–53, Feb. 2012.

[55] M. Ciobotaru, R. Teodorescu, and F. Blaabjerg, "A new single-phase PLL structure based on second order generalized integrator," *Proc. IEEE PESC*, pp. pp. 1–6, June 2006.

[56] K. Możdżyński, K. Rafał, and M. Bobrowska-Rafał, “Application of the second order generalized integrator in digital control systems,” *Archives of Electrical Engineering*, vol. 63, no. 3, pp. 423–37, Sep. 2014.

[57] Y. Xiao, and Y. Tadokoro, “LMS-based notch filter for the estimation of sinusoidal signals in noise,” *Signal Processing*, vol. 46, no. 2, pp. 223–31, Oct. 1995.

[58] J. G. Webster, “Reducing motion artifacts and interference in biopotential recording,” *IEEE Trans. Biomed. Eng.*, vol. 31, no. 12, pp. 823–26, Dec. 1984.